Earth and Space Science

RESEARCH ARTICLE
10.1029/2024EA003880

Local Time Variations of Quiet Time Meridional Winds During Solar Minimum Solstices Based on ICON Observations and Numerical Simulations

Tingting Yu[1,2,3,4], **Xuguang Cai**[5], **Zhipeng Ren**[1,2,3], **Huixin Liu**[4], **Liuhui Qiu**[4], **Han Ma**[1,2,3,4], **Shaoyang Li**[1,2,3], **and Kun Wu**[6]

[1]Key Laboratory of Earth and Planetary Physics, Institute of Geology and Geophysics, Chinese Academy of Sciences, Beijing, China, [2]Beijing National Observatory of Space Environment, Institute of Geology and Geophysics, Chinese Academy of Sciences, Beijing, China, [3]College of Earth and Planetary Sciences, University of the Chinese Academy of Sciences, Beijing, China, [4]Department of Earth and Planetary Science, Kyushu University, Fukuoka, Japan, [5]Laboratory of Atmospheric and Space Physics, University of Colorado Boulder, Boulder, CO, USA, [6]School of Physics and Electronic Sciences, Changsha University of Science and Technology, Changsha, China

Key Points:
- ICON-observed F-layer meridional winds show that diurnal and semi-diurnal variations dominate at ~20°N–40°N and 10°S–~20°N respectively
- In June, pressure gradient force dominated the semi-diurnal variation, and Coriolis force had a leading role in the diurnal variation
- Semi-diurnal variations of meridional winds at low latitudes in June were more affected by upward propagating tides than those in December

Correspondence to:
Z. Ren and X. Cai,
zpren@mail.iggcas.ac.cn;
cxg1106@msn.cn

Citation:
Yu, T., Cai, X., Ren, Z., Liu, H., Qiu, L., Ma, H., et al. (2025). Local time variations of quiet time meridional winds during solar minimum solstices based on ICON observations and numerical simulations. *Earth and Space Science*, *12*, e2024EA003880. https://doi.org/10.1029/2024EA003880

Received 15 JUL 2024
Accepted 19 JAN 2025

Author Contributions:
Conceptualization: Xuguang Cai
Formal analysis: Tingting Yu
Funding acquisition: Zhipeng Ren
Investigation: Tingting Yu
Methodology: Xuguang Cai
Project administration: Zhipeng Ren
Resources: Huixin Liu
Supervision: Zhipeng Ren
Validation: Xuguang Cai, Huixin Liu, Kun Wu
Writing – original draft: Tingting Yu
Writing – review & editing: Xuguang Cai, Zhipeng Ren, Huixin Liu, Liuhui Qiu, Han Ma, Shaoyang Li

Abstract

ICON observations were used to investigate local time (LT) and latitudinal variations of thermospheric meridional winds in the middle-high thermosphere (160–300 km) during quiet times in 2020 June and December. At middle-low latitudes (10°S–40°N), meridional winds were predominantly equatorward in the summer hemisphere while mostly poleward in the winter hemisphere. The meridional winds showed that the diurnal variation was dominant between ~20°N and ~40°N, but the semi-diurnal variation played a leading role at lower latitudes (below ~20°N) during solstice months. Thermosphere-Ionosphere Electrodynamics General Circulation Model reproduced the ICON observed meridional wind variations qualitatively. A model diagnostic analysis shows that the pressure gradient force dominated the semi-diurnal variation of the winds, while the Coriolis force played a leading role in the diurnal variation in June. In December, LT variations of meridional winds were primarily driven by pressure gradient and ion drag forces. During both months, the vertical viscosity was important, tending to balance the effects of pressure gradients. Additionally, semi-diurnal variations of low-latitude meridional winds in June were more affected by upward propagating tides than those in December.

1. Introduction

Thermospheric neutral winds play a significant role on the state of the coupled Ionosphere-Thermosphere (IT) system. They drive ionospheric and thermospheric structures through electrodynamic and hydrodynamic processes of the I-T system (Jiang et al., 2021; Richmond & Roble, 1987; Yu et al., 2022, 2023). Specifically, neutral winds can redistribute the thermospheric mass, momentum and energy, and transport plasma along magnetic field lines or generate electric fields through the wind dynamo to modify the ionosphere (Cai et al., 2022a, 2022b; Chen et al., 2024 ; Kuai et al., 2025; Richmond, 1989; Wu et al., 2023, 2025; Yamazaki & Richmond, 2013; Zhai et al., 2024). Meridional winds are particularly crucial to understand the latitudinal variations of IT parameters and contribute to the thermal structure by the adiabatic heating and cooling process (Gasperini et al., 2016; Yu et al., 2021a, 2021b).

For decades, extensive efforts have been made to extend our understanding of the thermospheric neutral winds via ground-based Fabry-Perot interferometers (FPI) (Biondi & Feibelman, 1968; Emmert et al., 2003; Fejer et al., 2002), incoherent scatter radar measurements (Balsley et al., 1976; Lei et al., 2007) and ionosondes (Liu et al., 2004; Luan et al., 2004). However, ground-based observations at a single point make it difficult to determine the wind patterns in the surrounding area. Additionally, accelerometers onboard low-Earth-orbiting LEO satellites can provide in-situ observations of neutral winds at satellite altitudes, as was demonstrated for the Dynamics Explorer 2 (DE2) (Spencer et al., 1982) and the CHAllenging Minisatellite Payload (CHAMP) mission (Liu et al., 2006; Xiong et al., 2016; Zhang et al., 2018). However, these measurements are limited to a single altitude and cannot provide altitude profiles of the winds. In contrast, optical measurements of airglow emissions captured by LEO satellites can measure neutral wind altitude profiles, as demonstrated by DE2 (Hays et al., 1981) and the Wind Imaging Interferometer (WINDII) (Emmert et al., 2001, 2004; Fejer et al., 2000; Shepherd et al., 1993).

These observed wind data are collected to develop an extensively used empirical wind model, namely the Horizontal Wind Model series (Drob et al., 2015; Emmert et al., 2008; Hedin et al., 1988, 1991), which provides a rough distribution of global horizontal winds despite data sparseness. Oberheide et al. (2011) developed the Climatological Tidal Model of the Thermosphere in neutral temperature and winds, covering the gaps from the lower thermosphere to satellite altitudes (80–400 km). Recently, the NASA Ionospheric Connection Explorer (ICON) satellite used the Doppler Asymmetric Spatial Heterodyne technique to make remote measurements of thermospheric neutral winds (Englert et al., 2007; Immel et al., 2017). This technique improves the Michelson interferometer used in WINDII, and can take simultaneous interferogram samples in different emission lines at various altitudes (Makela et al., 2021). Additionally, compared with the CHAMP in situ measurements, ICON observed horizontal winds provide us a great opportunity to analyze the altitude variations of wind structures.

During geomagnetically quiet conditions, neutral winds primarily depend on horizontal pressure gradients and ion drag force, which are driven by solar extreme ultraviolet (EUV) radiation inputs and the neutral-ion collisions, respectively (Kelley, 2009; Qian et al., 2016). Additionally, the magnitudes of Coriolis force and vertical viscosity force are sometimes comparable with pressure gradients and ion drag (Killeen & Roble, 1984). The variation characteristics and physical mechanisms for the thermospheric winds have been investigated through observations and numerical models. For example, Liu et al. (2006) presented the climatology characteristics of equatorial zonal winds in ~400 km altitude based on CHAMP observations. Using ionosonde data, the day-night, seasonal, and solar cycle variations of the meridional winds have been investigated by Buonsanto (1990, 1991) and Liu et al. (2003, 2004). Lei et al. (2007) studied local time (LT) variations of thermospheric winds at Shigaraki station using the middle and upper atmosphere (MU) radar observations and simulations. Jiang et al. (2018) reported the LT, seasonal, and longitudinal dependencies of quiet-time horizontal winds at three mid-latitude stations at ~250 km using FPI observations and empirical and numerical models. Luan and Solomon (2008) investigated the longitudinal variations in meridional winds, retrieved from peak heights and density in F_2 layer observed by the Constellation Observing System for Meteorology, Ionosphere, and Climate (COSMIC) satellites. Yiğit et al. (2022) used ICON/MIGHTI observations to investigate the climatology in the neutral winds at low and middle thermosphere (90–200 km) during solstices. Gasque et al. (2024) presented the LT distribution of the meridional winds in the *F* region based on ICON/Michelson Interferometer for Global High-resolution Thermospheric Imaging (MIGHTI) measurements, and focused on the solar terminator wave structures of the thermospheric winds. The physical mechanisms responsible for thermospheric winds have been studied through a quantitative examination of the terms in the momentum equations using theoretical models, with a primary focus on variations at high latitudes (e.g., Killeen & Roble, 1984, 1986; Kwak & Richmond, 2007; Larsen & Mikkelsen, 1983; Mikkelsen & Larsen, 1983). Thus, detailed forcing terms driving the LT variation of the neutral winds and their latitudinal and altitudinal dependencies near mid and low latitudes have not been well addressed.

In this study, we report the LT variations of meridional winds in the mid-high thermosphere (160–300 km) using ICON observations between 10°S and 40°N during June and December under geomagnetically quiet conditions. The diurnal and semi-diurnal variations in meridional winds were reproduced qualitatively by the National Center for Atmospheric Research Thermosphere-Ionosphere Electrodynamics General Circulation Model (TIEGCM). A diagnostic package of TIEGCM was applied to research the physical mechanisms driving the meridional winds. Additionally, impacts from upward propagating tides on the LT variations have also been investigated through the controlled numerical experiments. Section 2 describes the ICON data and TIEGCM. Section 3 shows the results and discussions. Section 4 presents the primary conclusions of this study.

2. Data and Model

2.1. ICON Data

The ICON satellite was launched on 10 Oct 2019 and orbits the Earth at ~600 km altitude. The MIGHTI onboard the ICON satellite (Englert et al., 2017; Makela et al., 2021) employs two interferometers, MIGHTI-A and MIGHTI-B, to sense the airglow in the red-line (630.0 nm) and green-line (557.7 nm) oxygen emissions on the dayside and nightside, covering ~12°S to 42°N latitudes. The neutral wind velocity can be retrieved along the line of sight from two MIGHTI instruments. Daytime wind data cover the altitude range of ~160–300 km from the red line emission, and the altitude range of 90–300 km from the green line (557.7 nm) emission. The temporal resolution of daytime wind profiles is 30 s. Nighttime wind data cover the altitude range of ~210–300 km from the red line emission and the altitude range of 90–110 km from the green line. The temporal resolution of nighttime wind profiles is 60 s. In this study, we used version v05 of the MIGHTI Level 2.2 data products of red-line neutral wind from 160 to 300 km during the day and night, and we removed the data with "bad" label according to the

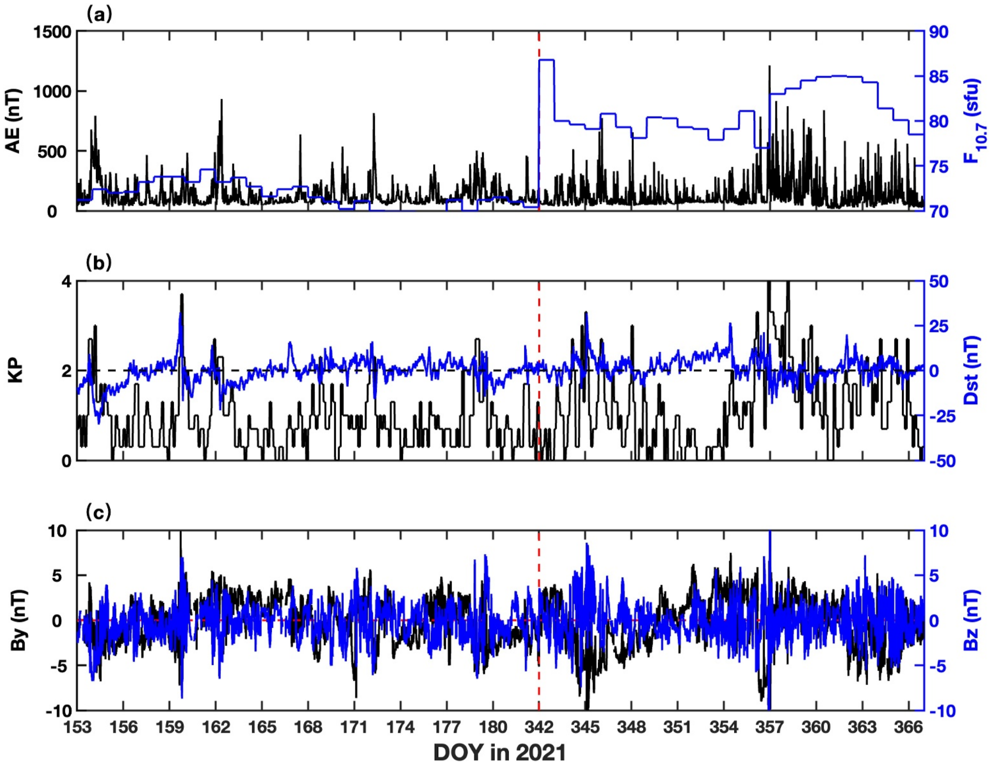

Figure 1. (a) Temporal variations in AE (black line) and $F_{10.7p}$ (blue line) indices in June and December in 2020; (b) Kp (black line) and Dst (blue line) indices, the black dashed line is the zero value of Dst; (c) B_y (black line) and B_z (blue line), and the dashed line is the zero value of B_y and B_z. The red vertical dashed lines divide June and December.

MIGHTI's data quality flags. This version was published in December 2022 and fills some long data gaps due to solar contamination. Furthermore, version v05 also incorporates the updates in the zero-wind calibration, the thermal drift correction and the pointing verification using star observations (Englert et al., 2023).

2.2. TIEGCM

NCAR TIEGCM is a first principles upper atmosphere general circulation model that self-consistently solves the momentum, energy, and continuity equations of the coupled IT system at each time step (Qian et al., 2014; Richmond et al., 1992; Roble et al., 1988). The vertical resolution of the model used here is 0.25 scale height with 57 constant pressure surfaces ranging from ∼97 to ∼600 km altitude, depending on solar activity. The horizontal resolution in latitude and longitude is 2.5° × 2.5°. In this study, the high-latitude inputs are provided by the Weimer model (Weimer, 2005), driven with the observed solar wind and interplanetary magnetic field (IMF) data. Two group runs were executed. One is with and another is without the monthly tidal climatology at the lower boundary from the two-dimensional, linear steady state global scale wave model (GSWM) (Hagan & Forbes, 2002, 2003). The time interval of simulation outputs is 1 hr with the complete runs in June and December in 2020. Additionally, the diagnostic package is used to calculate the acceleration terms in the momentum equation (Killeen & Roble, 1984, 1986).

3. Results and Discussions

3.1. Geomagnetic Conditions

Figure 1 presents the temporal variation of AE, $F_{10.7}$, Kp, Dst and IMF B_y and B_z in 2020 June and December. AE and Dst indices can be downloaded in https://supermag.jhuapl.edu/indices/. $F_{10.7p}$, Kp, B_y and B_z indices are from https://cdaweb.gsfc.nasa.gov/cdaweb/sp_phys/. AE and Kp indices were less than 1,000 nT and 4, respectively, except on DOY 356 and 358. Thus, we removed these two days from the statistical analysis of the meridional winds. The absolute values of Dst were mostly less than 25 nT. B_y and B_z exhibited small disturbances within

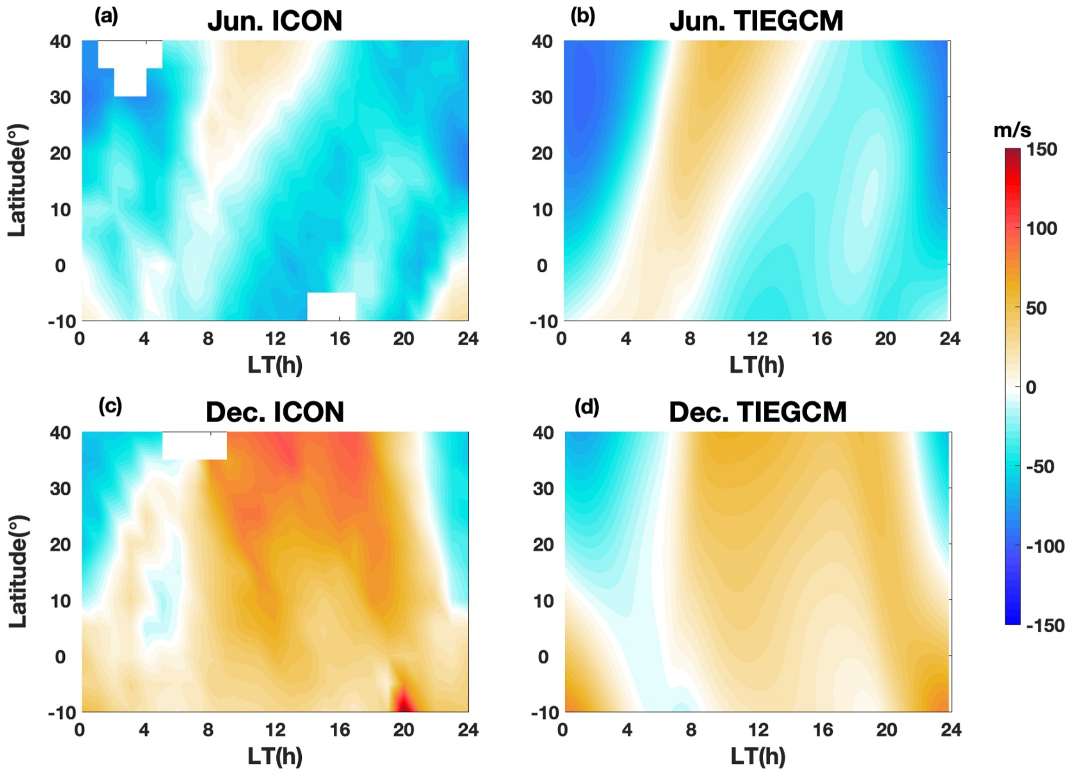

Figure 2. Local time (LT) (0–24 LT) and latitudinal (10°S–40°N) distribution of the meridional winds at 253.7 km in June and December from ICON observations (a, c) and Thermosphere-Ionosphere Electrodynamics General Circulation Model simulations (b, d). Positive (negative) values stand for northward (southward) winds.

~10 nT. In June, $F_{10.7}$ varied between 69 and 75 sfu with a monthly average value of 71.7 sfu. In December, $F_{10.7}$ in the first five days (DOY 336–341) are 101.2, 101.9, 99.9, 93, 97, 88.2 sfu, respectively, which are much larger than that in the other days of December (between 78 and 86). Thus, we removed the first days of December (DOY 336–341). The averaged $F_{10.7}$ in the rest of December is 81.1 sfu. Overall, these 2 months are pretty quiet.

3.2. Data/Model Comparison

The monthly and longitudinal mean of meridional winds was calculated to present the LT and latitude dependence of the wind profiles from ~160 to 300 km at 10°S–40°N latitude. The meridional winds were binned into 1-hr LT intervals and 5° latitude bins. An altitude of ~250 km was chosen to show the LT and latitude distribution of meridional winds in ICON observations (left column) and TIEGCM simulations (right column) in June and December in Figure 2. In the North Hemisphere (NH), positive values stand for poleward (northward) meridional winds, and negative values are equatorward (southward) meridional winds.

In June (Figure 2a), ICON observations indicate that meridional winds in the NH were mostly equatorward (southward) in the night sector with the maxima of ~90 m/s. Poleward (northward) winds only existed between ~8 and ~14 LT at 40°N with the maxima of ~30 m/s, and their LT range shortened with the decrease of latitude. By ~10°N to 0°, the poleward winds were almost entirely replaced by the equatorward winds in all LTs. The wind direction switch was latitude-dependent, tending to occur at earlier LTs with the decreasing latitude. In the Southern Hemisphere (SH), meridional winds were equatorward (northward) near local midnight (~22–~2 LT), reaching the maxima of ~30 m/s. Poleward (southward) winds were prevalent during the daytime and other nighttime LTs, with the maxima of ~80 m/s. Additionally, the meridional winds showed an obvious diurnal variation above ~20°N, and a semi-diurnal variation dominated at lower latitudes (from ~20°N to 10°S). Taking ~10°N for instance, the meridional winds had a maximum at ~8 LT (northward, ~30 m/s) and ~19 LT (southward, ~10 m/s), and a minimum at ~15 LT (southward, ~60 m/s) and ~21.5 LT (southward, ~70 m/s).

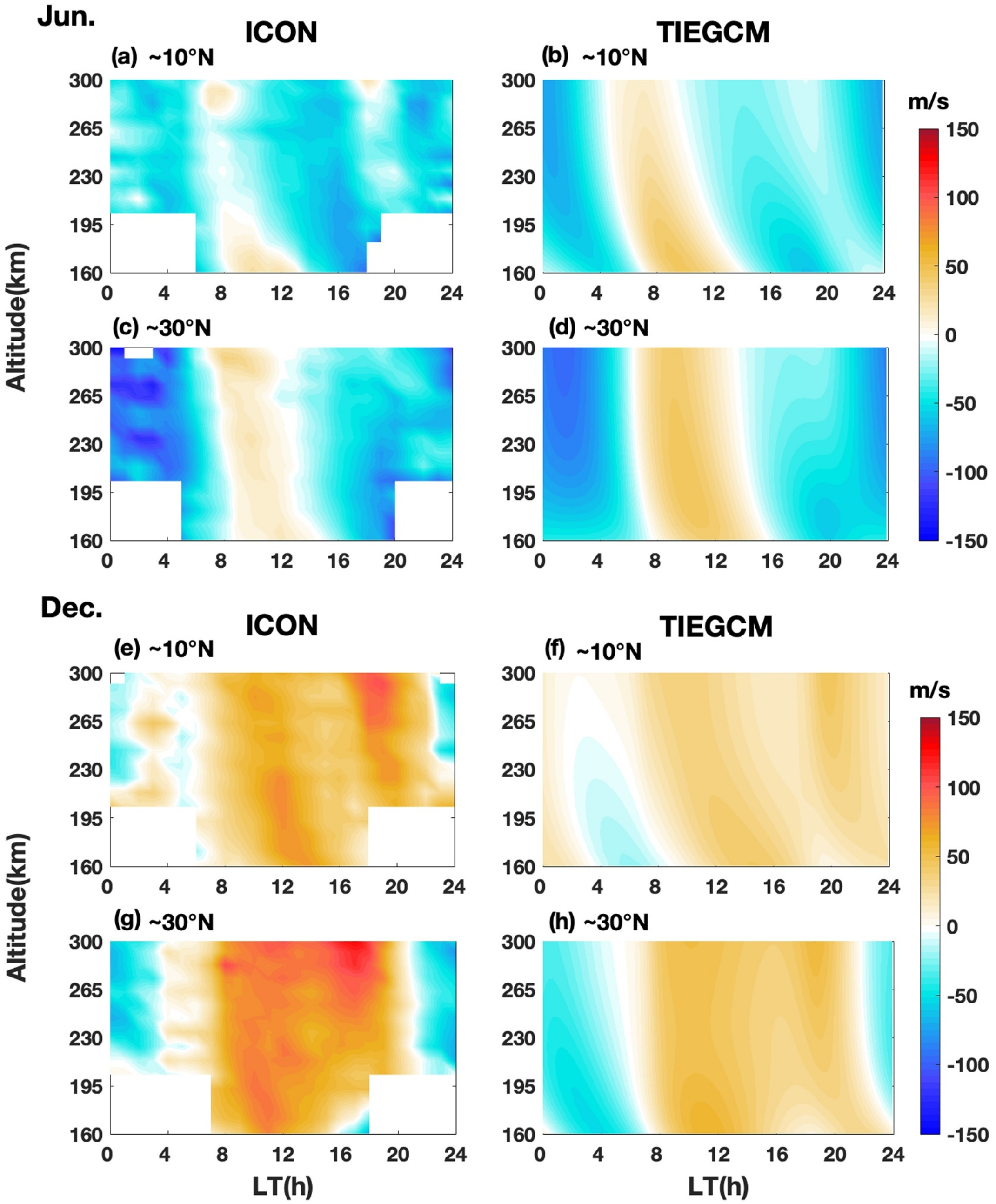

Figure 3. (a–d): Local time (LT) (0–24 LT) and altitude (160–300 km) distribution of the meridional winds at ∼10°N and ∼30°N in June from ICON observations and Thermosphere-Ionosphere Electrodynamics General Circulation Model simulations; (e, f): same to (a–d), but in December.

In December (Figure 2c), ICON observations indicate that meridional winds in the NH were mostly poleward (northward), and the LTs varied from ∼5 to ∼21 LT at 40°N to ∼0–∼24 LT at 10°N, extending to the equator. The maxima of poleward winds were ∼160 m/s, decreasing with the latitudes. Equatorward (southward) winds occurred at other LTs with the maxima of ∼70 m/s. In the SH, equatorward (northward) winds were observed at all LTs. In December, the diurnal variations were also distinct above ∼20°N, and a semi-diurnal variation was dominant at lower latitudes (from ∼20°N to 10°S). Taking ∼10°N for instance, the meridional winds had a maximum at ∼12 LT (northward, ∼80 m/s) and ∼18.5 LT (northward, 80 m/s), and a minimum at ∼6 LT (southward, ∼30 m/s) and ∼15 LT (northward, ∼30/s). Wind directions in June and December illustrate that the observed wind circulation features are mostly consistent with the simulated results in Rishbeth and Müller-

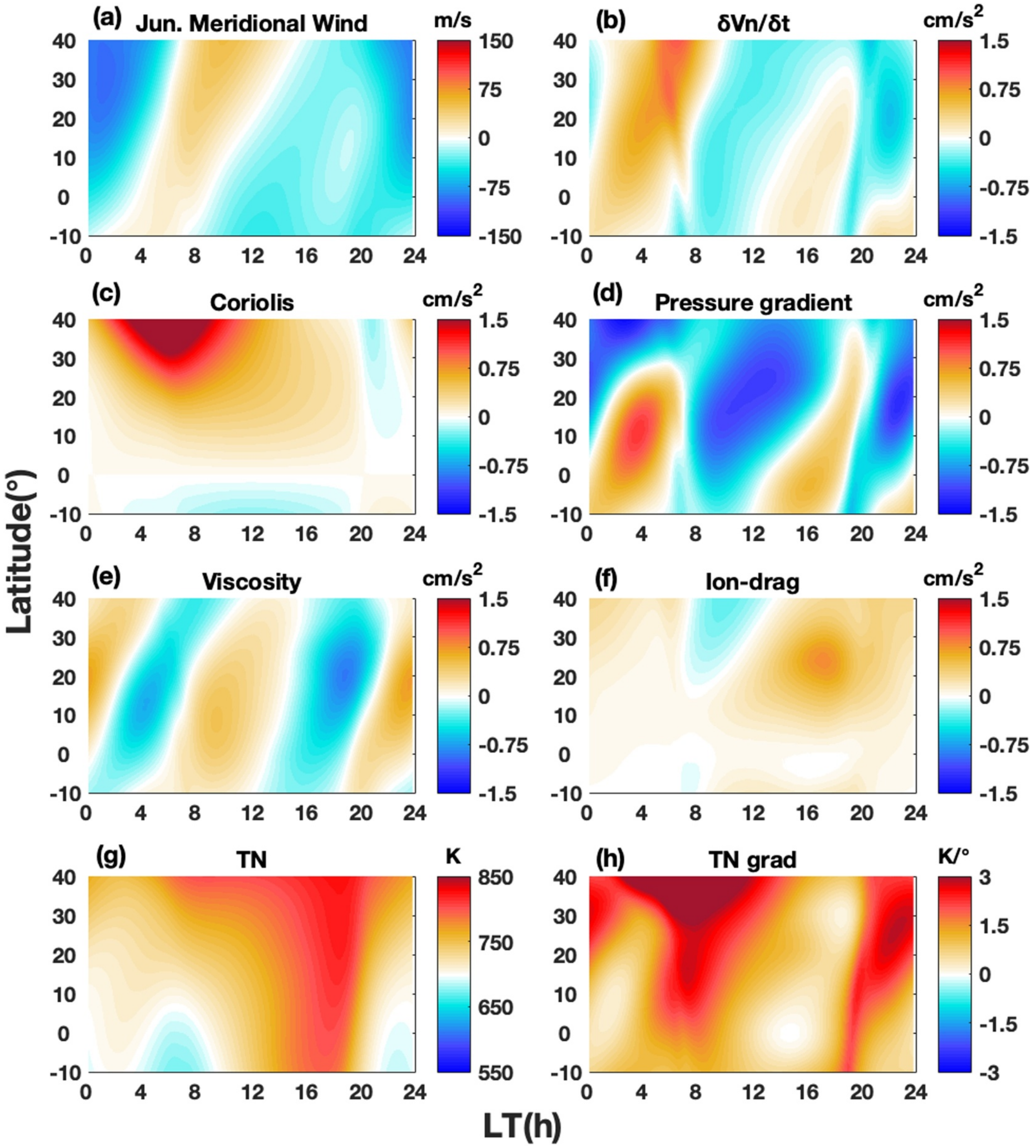

Figure 4. Local time (LT) (0–24 LT) and latitudinal (10°S–40°N) distribution in V_n (meridional wind speed) (a), the total time rate of change of V_n ($\partial V_n/\partial t$) (b), Coriolis force (c), pressure gradient (d), vertical viscosity (e), and ion drag force of V_n (f); neutral temperature (TN) (g) and latitude gradient of TN (h) at 253.7 km in June.

Wodarg (1999) (Figure 1). Yamazaki et al. (2023) used the same ICON/MIGHTI data to analyze the amplitudes of different tidal composition in F-layer meridional winds. The results show that diurnal variation dominated at higher latitudes and semi-diurnal variation dominated at lower latitudes, which is consistent with our results. Additionally, the maximum and minimum occurred around the evening terminator indicated the existence of solar terminator waves; for more details, see Gasque et al. (2024).

In TIEGCM simulations (Figures 2b and 2d), the LT and latitude distribution in June is generally similar to that of ICON observations. TIEGCM reproduced the equatorward meridional winds in the NH in the nightside with the similar maxima of ~90 m/s. The northward winds occurred over a larger LT range from ~7 LT to ~15 LT at 40°N, with the maxima of ~50 m/s, which was larger than the observed results (~30 m/s). The LT range of these winds also shrank with decreasing latitude but extended to approximately 10°S, ranging from around 3 LT to 7 LT. In the SH, the equatorward (northward) observed winds near midnight were not modeled by TIEGCM. TIEGCM reproduced the observed diurnal and semi-diurnal variations and their latitude dependency. Taking

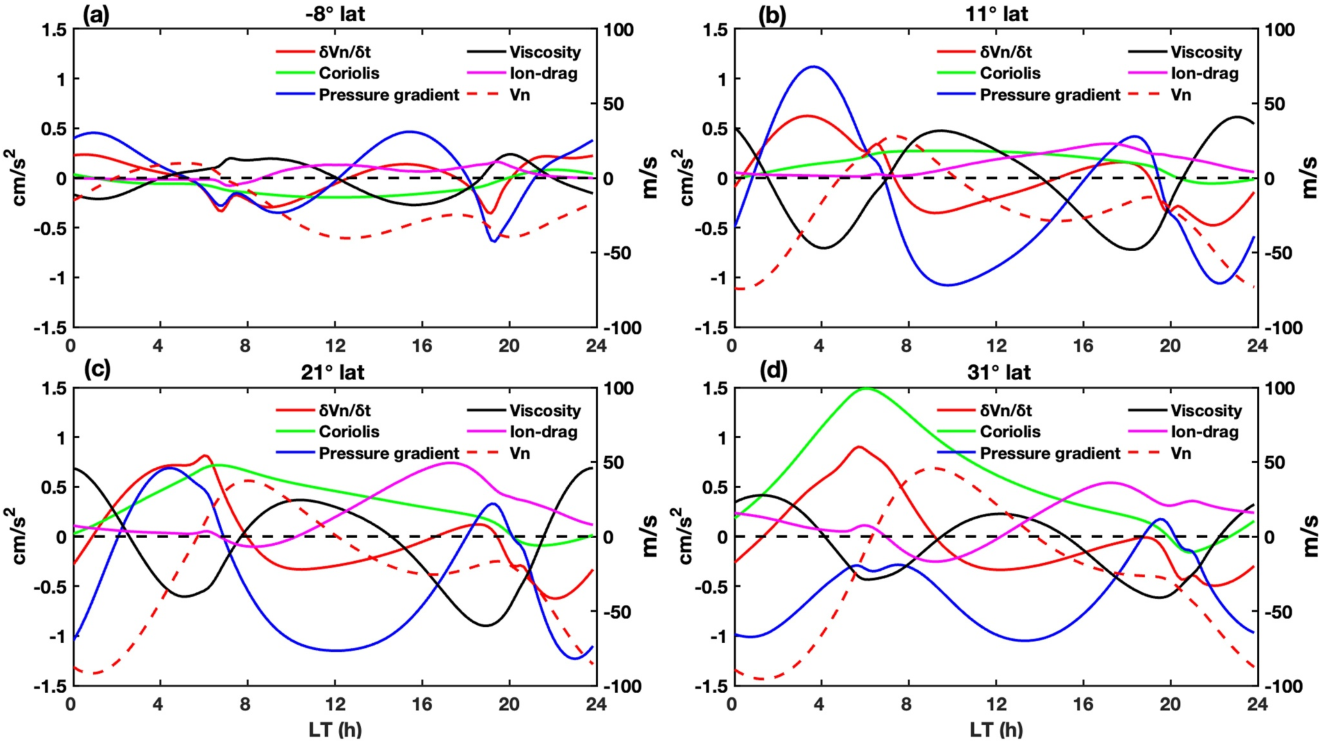

Figure 5. Local time variations in the total time rate of change of V_n ($\partial V_n/\partial t$), Coriolis force, vertical viscosity, ion drag and pressure gradient force of V_n at the latitude of ~8°S (a), ~10°N (b), ~20°N (c), and ~30°N (d) at 253.7 km in June.

~10°N for instance, TIEGCM simulated winds showed two maxima at ~8 LT (northward, ~30 m/s) and ~19 LT (southward, ~15 m/s), and two minima at ~15 LT (southward, ~30 m/s) and ~0 LT (southward, ~75 m/s) (see Figure 5b). Compared with the observations, TIEGCM underestimated the magnitude of the southward wind minimum at ~15 LT. In December, TIEGCM simulations also reproduced the meridional wind direction and LT distributions. However, the semi-diurnal variations occurred at all latitudes, differing from the observations that only exhibited this feature at lower latitudes (~20°N to 10°S). Additionally, the magnitudes of the meridional wind are different with the maxima of ~80 m/s in northward winds (lower than the observations of ~160 m/s), and the maxima of ~60 m/s in southward wind (lower than the observations of ~70 m/s).

Figure 3 presents the LT and altitude distribution of meridional winds at ~10°N and ~30°N in June and December from ICON observations and TIEGCM simulations. Note that there are no nighttime wind observations in 160–210 km altitude range mentioned in Section 2. In general, the simulation results match the ICON observations well, though there were still some magnitude differences. As aforementioned, the semi-diurnal variations were more obvious at lower latitudes (~10°N) both in June and December. The observations and simulations show that the diurnal and semi-diurnal variation were evident at all altitudes from 160 to 300 km. Additionally, the maxima (minima) of the winds drifted to earlier LTs with the increasing height during both months. In summary, the basic distribution of meridional winds in LT, latitude and altitude are reproduced qualitatively by TIEGCM, though with some discrepancies. Therefore, the model outputs can be utilized to investigate the physical mechanisms of the wind patterns under quiet conditions.

3.3. Forcing Terms of Meridional Winds

A diagnostic term-by-term analysis (Killeen & Roble, 1986; Yu et al., 2022) was performed for the model outputs. The meridional momentum equation is given as:

$$\frac{\partial V_n}{\partial t} = \frac{ge^z}{P_0}\frac{\partial}{\partial z}\left[\frac{\mu \partial V_n}{H\partial Z}\right] - f^{\mathrm{cor}}U_n + \lambda_{yy}(V_i - V_n) + \lambda_{yx}(U_i - U_n) - V_n\cdot\nabla V_n + \frac{U_n U_n}{R_E}\tan\lambda - \frac{1}{R_E}\frac{\partial\Phi}{\partial\lambda} - W_n\frac{\partial V_n}{\partial Z}$$

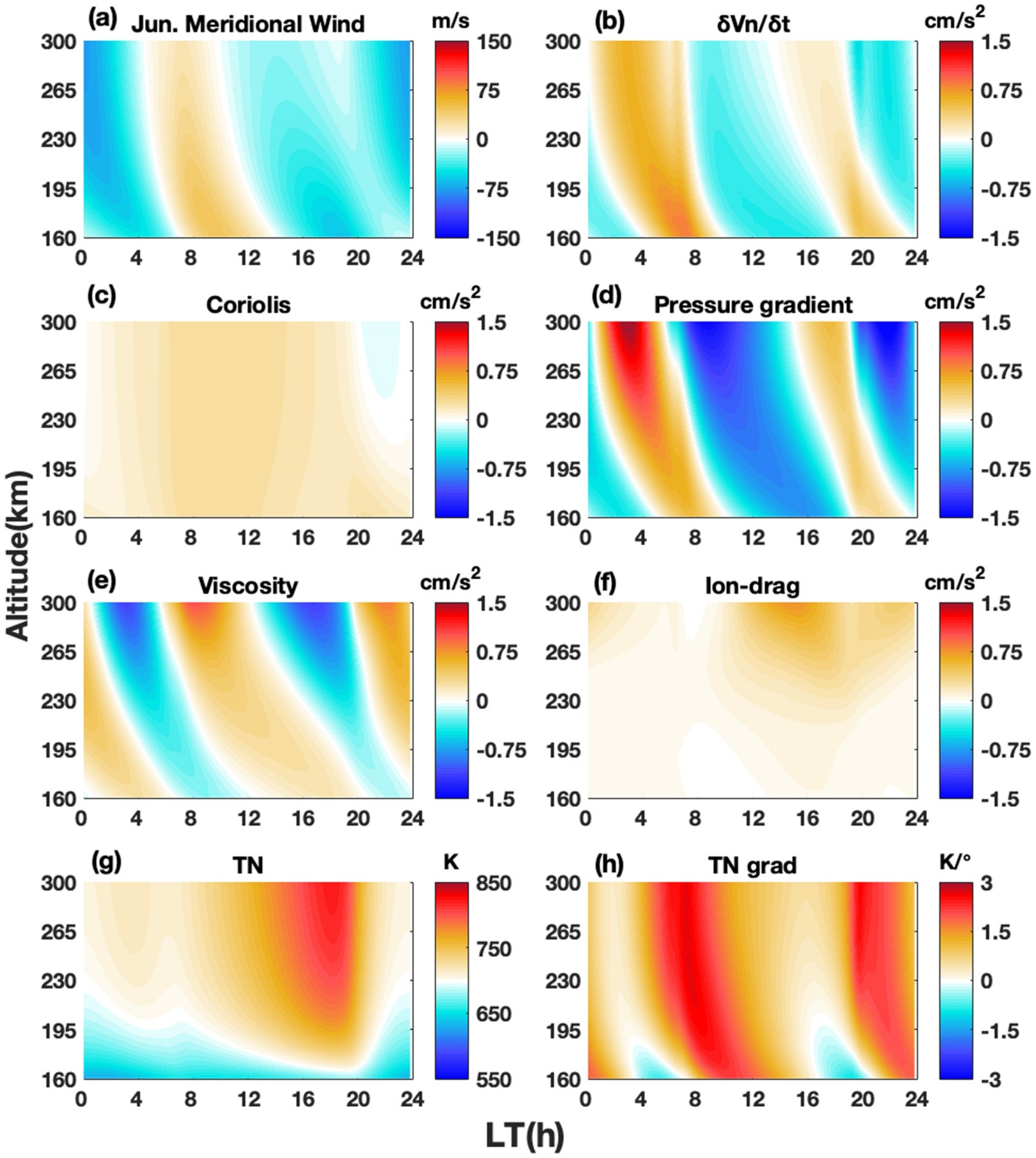

Figure 6. Local time (LT) (0–24 LT) and altitude (160–300 km) distribution in V_n (meridional wind speed) (a), the total time rate of change of V_n ($\partial V_n/\partial t$) (b), Coriolis force (c), pressure gradient force (d), vertical viscosity (e), and ion drag force of V_n (f); neutral temperature (TN) (g) and latitude gradient of TN (h) at ~10°N in June.

where V_n are meridional wind speeds, t is time, $\partial V_n/\partial t$ is total meridional acceleration, g is the gravitational acceleration, P_0 is the reference pressure, μ is the viscosity coefficient, H is the pressure scale height, f^{cor} is the Coriolis parameter, λ_{yx} and λ_{yy} are ion drag coefficients, U_i and V_i are zonal and meridional velocities of ion, R_E is Earth radius, Φ is air pressure, λ is latitude and W_n is the vertical wind. According to the meridional momentum equation, the total meridional acceleration ($\partial V_n/\partial t$) is determined by terms on the right-hand side of the equation: vertical viscosity, Coriolis force, ion drag force, horizontal momentum advection, centrifugal force, pressure gradient force, and vertical momentum advection. As demonstrated by previous studies (Wang et al., 2008; Yu et al., 2022), the contributions from vertical momentum advection, horizontal momentum and centrifugal force are insignificant and can be ignored.

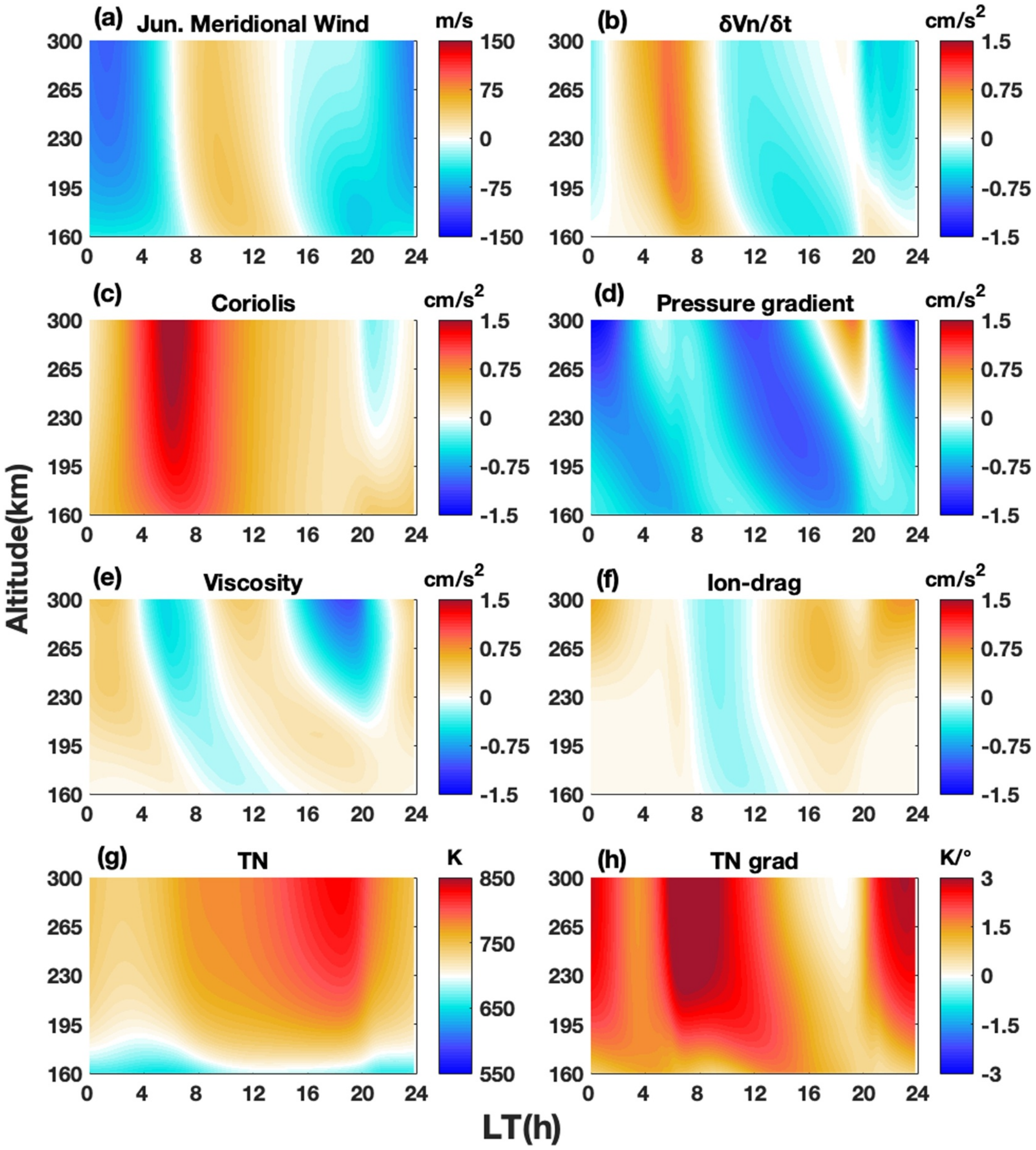

Figure 7. Same to Figure 6, but at ~30°N in June.

Net positive (negative) acceleration could increase (reduce) the northward meridional wind speed, but reduce (increase) the southward wind speed. It is worth noting that the forcing terms impact wind speed in an accumulative way, but net acceleration represents the instantaneous force at one time. The relative contributions of forcing terms can be seen by the comparison of magnitude and distribution with $\partial V_n/\partial t$.

Figure 4 show the LT and latitude distribution of the other four total forces and total acceleration, and the wind variations at ~250 km in June. The neutral temperature and its latitudinal gradient distribution are also provided in Figures 4g and 4h. To assess the forcing magnitudes of the meridional winds intuitively, the fixed latitudes (~8°S, ~10°N, ~20°N, ~30°N) are chosen to show the line plots in different LTs of these acceleration terms in Figure 5. In June, the pressure gradient force was a primary forcing mechanism in meridional winds at ~250 km below ~20°N at all LTs. Between ~20°N and 40°N, ~1–~12 LT, the Coriolis force had a significant positive effect on the acceleration term. The LT distribution of these terms indicated that the pressure gradient force dominated the semi-diurnal variations at lower latitudes (below ~20°N; see Figures 4b and 4d). Note that the pressure gradient

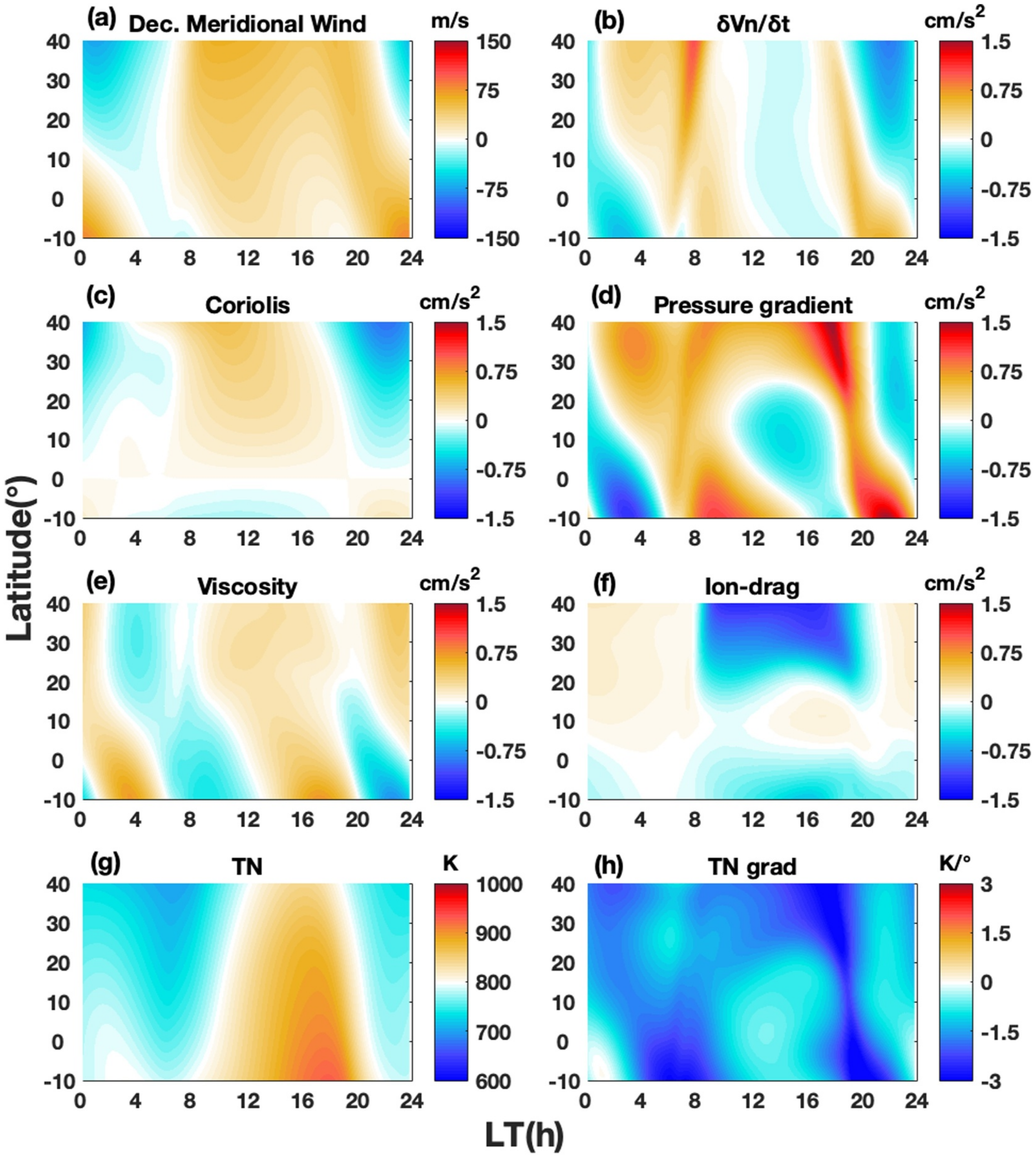

Figure 8. Same to Figure 4, but in December.

force is mainly produced by the temperature gradient, thus the latitudinal gradient pattern of the temperature (Figure 4h) was similar to that of the pressure gradient (Figure 4d). The semi-diurnal variations in temperature gradient (Figure 4h) are primarily driven by the large temperature changes during sunrise and sunset. These temperature changes appear to influence summer meridional winds at lower latitudes, suggesting a connection between the diurnal cycle and wind behavior. Furthermore, the large temperature variations near the terminator and the resulting pressure gradient force likely play a key role in the formation of solar terminator waves (Gasque et al., 2024). Meanwhile, between ∼20°N and 40°N, the diurnal variations were mainly determined by the Coriolis force, as shown in Figures 5c and 5d, which had an enhancement with the increased latitudes. The ion drag term was relatively smaller in June. Thus, the interplay of pressure gradient and Coriolis force as well as vertical viscosity dominated meridional wind variations in the middle-high thermosphere in June.

Figures 6 and 7 present the LT and altitude distribution of these terms at latitudes of ∼10°N and ∼30°N in June. At ∼10°N, the magnitude of the Coriolis force and ion drag force was relatively small. The pressure gradient force

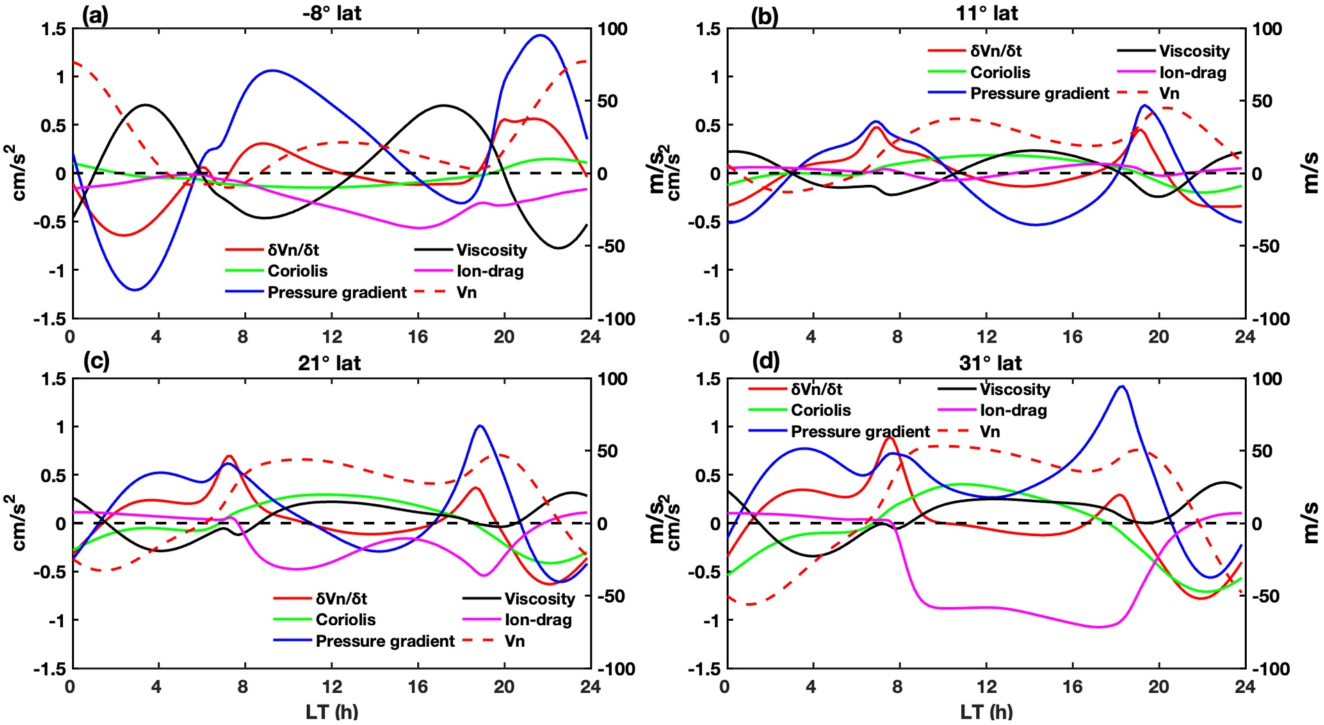

Figure 9. Same to Figure 5, but in December.

and the vertical viscosity force had an enhancement with increasing height. At ∼30°N, the direction of the pressure gradient force reversed from southward to northward after sunset at ∼230 km with increasing height. The direction of the vertical viscosity force at ∼30°N reversed from northward to southward after sunset at ∼200 km with increasing height. Additionally, the magnitude of the viscosity force increases with height due to the decrease of the neutral densities with height, which usually acted to smooth out the vertical changes of winds (Wang et al., 2008). Before local noon (∼12 LT), the positive Coriolis forces increased with the altitude, dominating the poleward winds and their diurnal variations.

Figure 8 show the distribution of the variables same to Figure 4 but in December. Additionally, the line plots at different latitudes are shown in Figure 9. In December, the pressure gradient force was also a dominant mechanism for the meridional winds at ∼250 km and was also closely related to their semi-diurnal variations at almost all latitudes. Additionally, ion drag force had a large negative effect on the acceleration term between ∼8 and ∼19 LT, especially above ∼20°N (Figure 9d). The magnitude of the ion drag force during the dayside is similar to that of pressure gradient and vertical viscosity forces. Thus, the interplay of pressure gradient and vertical viscosity as well as the ion drag forces dominated the meridional wind variations in *F* height in December. The ion drag term is connected with the collision frequency between ion and neutral components, neutral winds and ExB drift velocities (Hsu et al., 2016). Therefore, fewer ions in the ionosphere during the nightside resulted in the weaker ion drag forcing than during the dayside (Wang et al., 2008). Additionally, the simulated semi-diurnal variations occurred at all latitudes, which were different from the observations that semi-diurnal variations only dominated at lower latitudes (∼20°N to 10°S). That indicated that the dominant forcing term of semi-diurnal variations above ∼20°N (pressure gradient force) may be overestimated by the simulation in December.

In December, TIEGCM simulations show the semi-diurnal variation of the wind at all latitudes, thus, one latitude (∼30°N) is chosen to present the LT and altitude distribution of these terms in Figure 10. The direction and magnitude of pressure gradients also depend on the altitude. The direction of pressure gradient force reverses from southward to northward at ∼180 km at ∼16 LT. At ∼18 LT, there was a maximum of positive pressure gradients above ∼260 km. Ion drag forces have no obvious direction differences with height, but increased in magnitudes with the increasing height. The most striking feature in the vertical viscosity forces is that they have a positive

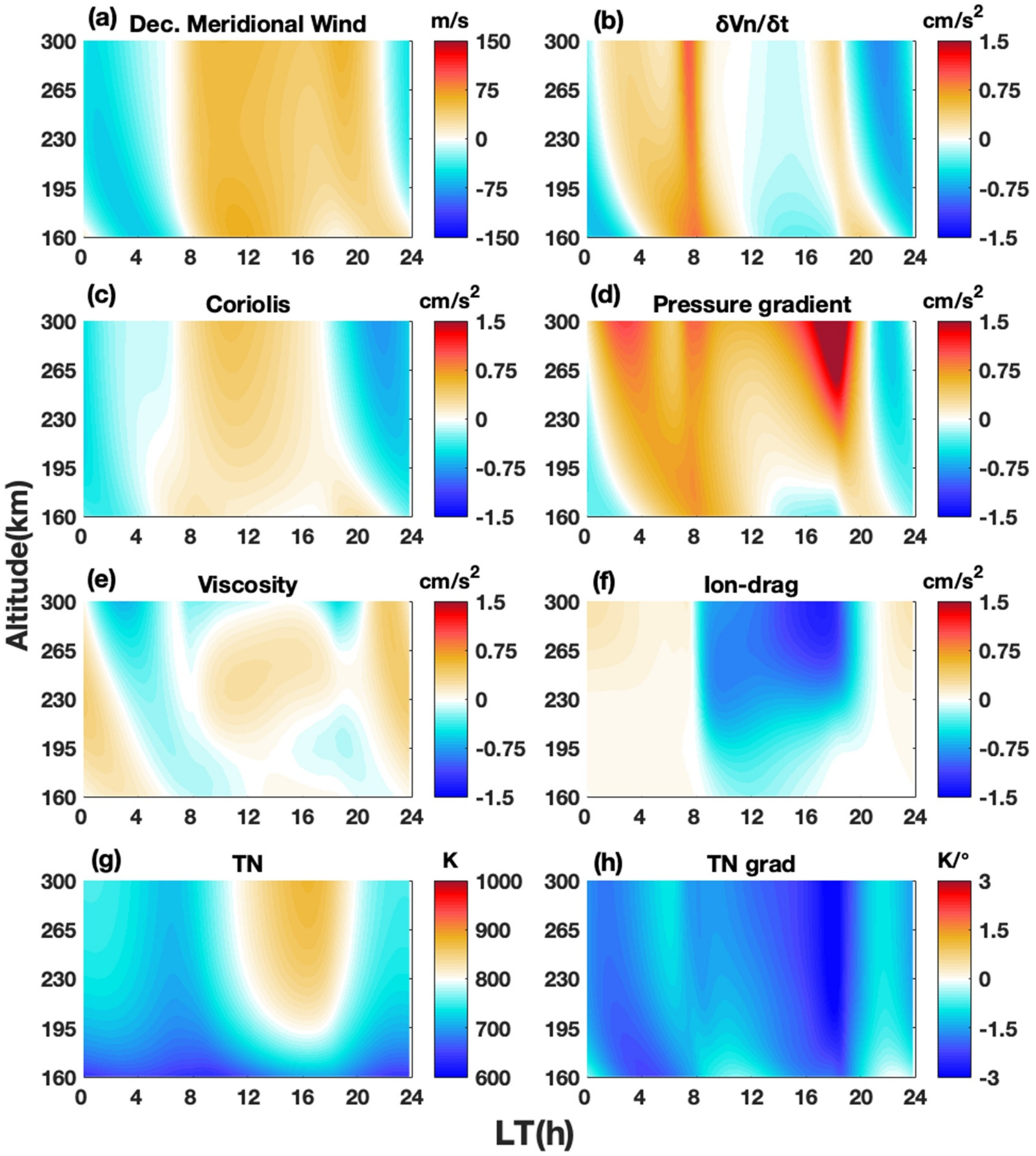

Figure 10. Local time (LT) (0–24 LT) and altitude (160–300 km) distribution in Vn (meridional wind speed) (a), the total time rate of change of V_n ($\partial V_n/\partial t$) (b), Coriolis force (c), pressure gradient force (d), vertical viscosity (e), and ion drag force of V_n (f); neutral temperature (TN) (g) and latitude gradient of TN (h) at ∼30°N in December.

maximum at ∼240 km at ∼10–∼18 LT, different from their continuous increases with height at all LTs in June. Additionally, the Coriolis forces also increased with the altitude.

The seasonal differences and directions of the wind field are attributed to the summer-winter pressure gradient induced by the higher neutral temperatures in the summer hemisphere (Figures 4g and 8g). Notably, the ion drag force was larger in December (winter hemisphere) compared to that in June (summer hemisphere), especially during daytime. During solstices, the large-scale interhemispheric circulation happens due to the uneven solar radiation between two hemispheres (Fuller-Rowell, 1998). Thus, the stronger upwelling in the summer hemisphere transports N_2-rich air up to upper thermosphere, leading to a lower O/N_2 in the local summer hemisphere than the local winter hemisphere (Burns et al., 2015; Qian et al., 2016; Yu et al., 2020). Note that electron production and loss result mainly from the photoionization of O and the dissociative recombination of O^+ with N_2 and O_2, respectively (Rishbeth, 1998; Yu et al., 2004). Thus, O/N_2 has a good correlation with the electron (ion)

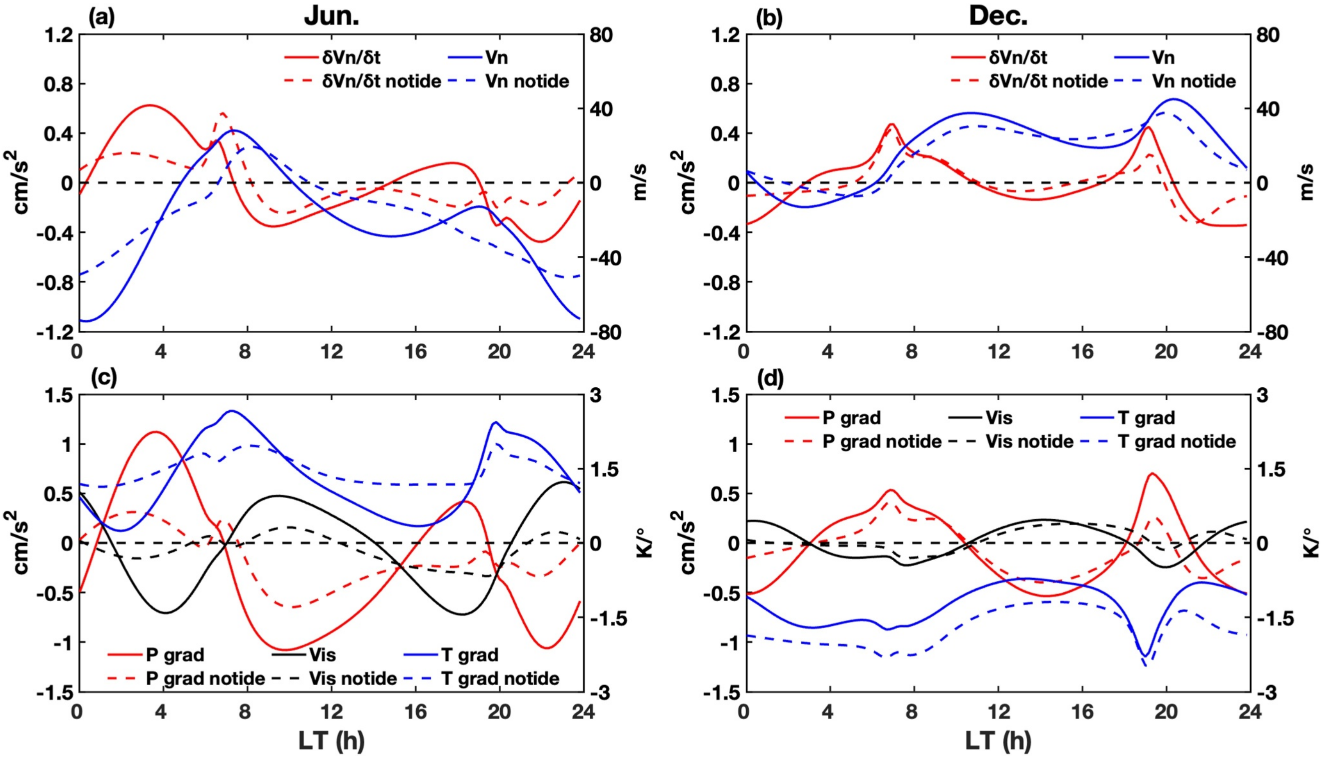

Figure 11. (a) Local time (LT) variations in V_n (blue lines) and the total time rate of change of V_n ($\partial V_n / \partial t$, red lines) with (solid lines) and without (dashed lines) tides at the latitude of ~10°N at 253.7 km in June; (b) same as (a) but in December; (c) LT variations in pressure gradient force (red lines) and vertical viscosity (black lines) of V_n, and the latitude gradient of neutral temperature (blue lines) with (solid lines) and without (dashed lines) tides at the latitude of ~10°N at 253.7 km in June; (d) same as (c) but in December.

density when O_2 is supposed to behave similarly to N_2 (Burns et al., 1995). This caused the higher electron (ion) density in the winter hemisphere, which was a factor in direct proportion to the ion drag force, and thus the larger ion drag force here.

3.4. Tide Effects on Meridional Winds

Besides the effects from the solar source, the neutral winds are also modified by the upward propagating tides at the middle-low atmosphere (e.g., Crowley et al., 1989). To test whether the tides impact the V_n pattern during the quiet time, we compare the LT variations of simulation results with and without upward propagating tidal forcing in Figure 11 (~10°N, ~250 km). The simulations without tidal forcing were run by excluding the bottom inputs of both migrating and non-migrating diurnal/semidiurnal tides.

In June (Figure 11a), the winds (blue dashed line) showed a stronger diurnal variation in the absence of upward propagating tides. Introducing tides into the simulations added a semi-diurnal variation in the winds, primarily manifesting as a second maximum near ~19 LT (blue solid line). Figure 11c shows that the wind maximum near ~19 LT was dominated by the large positive pressure gradient force values with tides (red solid line), which changed to less negative values without tides (red dashed line). This was also related to the changes in the latitudinal gradient of temperature (blue lines in Figure 11c) (Jones et al., 2016). Therefore, the upward propagating tides modify the pressure gradient force to control the semi-diurnal variations in summer meridional winds at lower latitudes. The semi-diurnal variations at lower latitude in June were mainly driven by the semi-diurnal tides, not the solar source. In December, the upward propagating tides had relatively less effects on the wind variations, and the semi-diurnal variations at lower latitudes were still existing without tidal forcing (Figure 11b). Thus, the semi-diurnal variations in winter solstice meridional winds were largely dominated by the solar heating and the resulting thermospheric temperature changes.

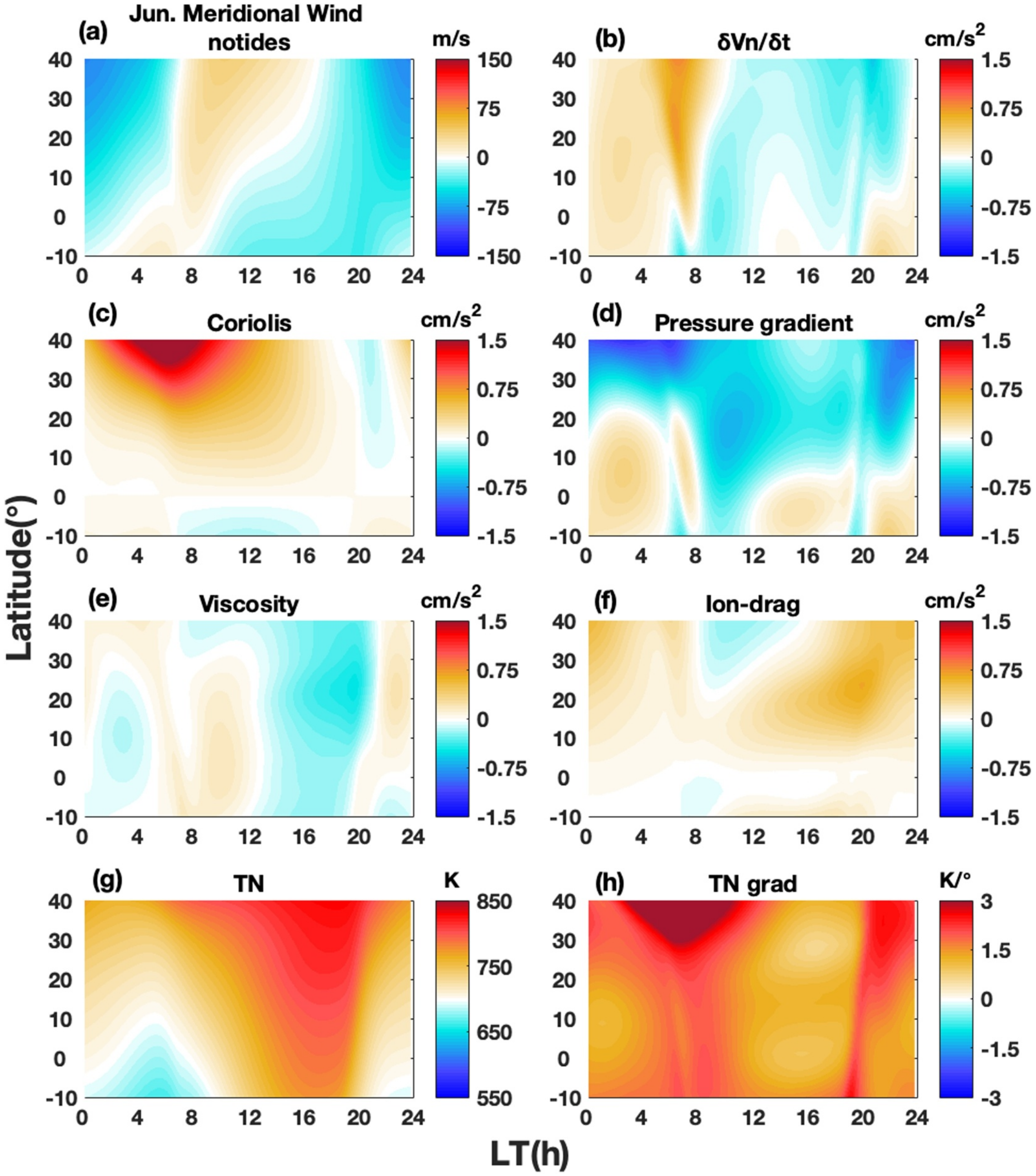

Figure 12. Local time (LT) (0–24 LT) and latitudinal (10°S–40°N) distribution in V_n (meridional wind speed) (a), the total time rate of change of V_n ($\partial V_n/\partial t$) (b), Coriolis force (c), pressure gradient force (d), vertical viscosity (e), and ion drag force of V_n (f); neutral temperature (TN) (g) and latitude gradient of TN (h) at 253.7 km in June without tides.

Figures 12 and 13 give the latitude distribution of the winds and the forcing terms without upward propagating tidal forcing. We still can see the larger effects of tides on the semi-diurnal variations in meridional winds at lower latitudes in June. The significant changes occurred on the pressure gradient and vertical viscosity force, while there were no large changes in other terms. Therefore, the winds at higher latitudes, which were mainly determined by the Coriolis force, still showed the similar diurnal variation characteristics compared with the results with tidal forcing. In December, all forcing terms had no evident changes when there were no upward propagating tides driving TIEGCM runs. Thus, the winds presented the similar latitude and LT distribution compared with the results with tidal forcing. Note that magnitude of the semi-diurnal tidal forcing (GSWM) in June and December has been verified to be similar. Namely, semi-diurnal variations of meridional winds at lower latitudes in June were more affected by upward propagating tides than those in December.

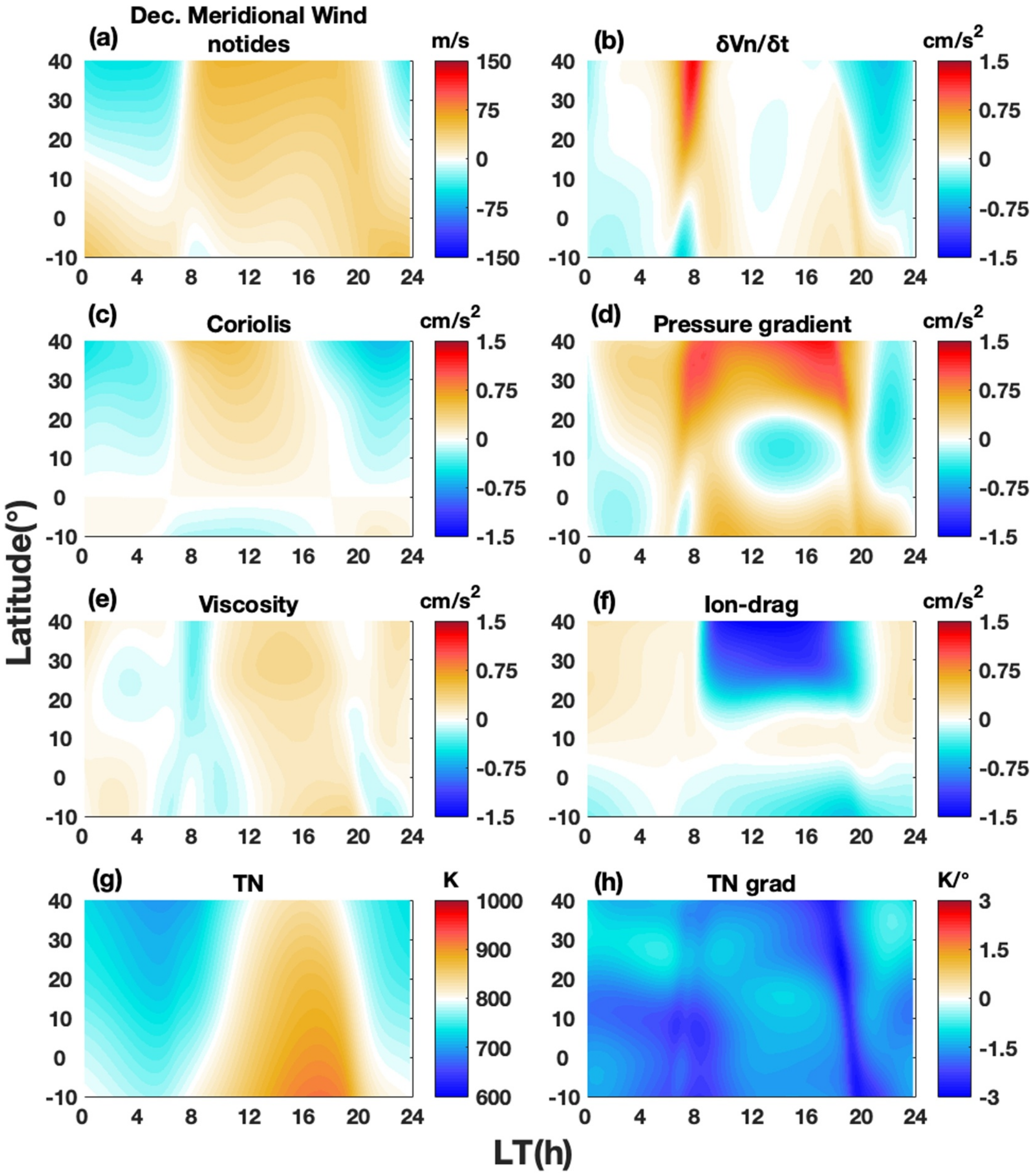

Figure 13. Same to Figure 12, but in December.

4. Conclusion

We report the LT (0–24 LT) and latitudinal (10°S–40°N) variations of meridional winds in *F* layer observed by ICON during quiet times in 2020 June and December, and investigate their physical mechanisms by TIEGCM simulations. Our main conclusions are summarized as follows:

1. During the solstice months in solar minimum, ICON observations show that meridional winds in the summer hemisphere are mostly equatorward. The LT ranges of dayside poleward winds, occurring ~8–~15 LT at 40°N, shrink with the decreasing latitude. The meridional winds in the winter hemisphere are predominantly poleward. The LT ranges of nightside equatorward winds that exist ~21–~5 LT at 40°N, also decrease with the latitude.
2. In both solstice months, the observed meridional winds show that the diurnal variation played a leading role between ~20°N and 40°N, but the semi-diurnal variation dominated at lower latitudes (from ~20°N to 10°S). TIEGCM simulated meridional winds were generally in good agreement with the ICON observations, though

there were some magnitude discrepancies. Additionally, the semi-diurnal variations occurred at all latitudes in the simulations in December.

3. TIEGCM simulations illustrate that the pressure gradient force was a major forcing mechanism for the meridional winds both in June and December, which mainly dominated the semi-diurnal variation of the winds. The vertical viscosity tended to balance the effects of pressure gradient force. However, in June, the Coriolis force had a large positive effect on meridional winds between 20°N and 40°N, which dominated the diurnal variation here. In December, the ion drag force had a large negative effect on the winds during the daytime.
4. The controlled simulations with and without tidal forcing show that the meridional winds at lower latitudes in June were more affected by the upward propagating tides compared with those in December. The upward propagating tides played a decisive role in the semi-diurnal variations of the winds at lower latitudes (~20°N to 10°S) in June.

Data Availability Statement

ICON data is from https://cdaweb.gsfc.nasa.gov/pub/data/icon/l2/l2-2_mighti_vector-wind-red/2020/. The data used in this article are available at in Yu (2024).

Acknowledgments
We thank the support from the B-type Strategic Priority Program of the Chinese Academy of Sciences (Grant XDB0780000), the National Key R & D Program of China (Grant 2022YFF0503901), B-type Strategic Priority Program of the Chinese Academy of Sciences (XDB41000000), National Science Foundation of China (42304178), China Scholarship Council, and China Meteorological Administration "Ionospheric Forecast and Alerting" Youth Innovation Team (CMA2024QN09). Xuguang Cai acknowledges the supports from National Science Foundation AGS-2437053. HL acknowledges support by JSPS Grants 20H00197, JP22K21345.

References

Balsley, B. B., Fejer, B. G., & Farley, D. T. (1976). Radar measurements of neutral winds and temperatures in the equatorial E region. *Journal of Geophysical Research*, *81*(7), 1457–1459. https://doi.org/10.1029/ja081i007p01457

Biondi, M. A., & Feibelman, W. A. (1968). Twilight and nightglow spectral line shapes of oxygen 6300 and 5577 radiation. *Planetary and Space Science*, *16*(4), 431–443. https://doi.org/10.1016/0032-0633(68)90158-X

Buonsanto, M. J. (1990). Observed and calculated F2 peak heights and derived meridional winds at mid-latitudes over a full solar cycle. *Journal of Atmospheric and Terrestrial Physics*, *52*(3), 223–240. https://doi.org/10.1016/0021-9169(90)90126-8

Buonsanto, M. J. (1991). Neutral winds in the thermosphere at mid-latitudes over a full solar cycle: A tidal decomposition. *Journal of Geophysical Research*, *96*(A3), 3711–3724. https://doi.org/10.1029/90JA02626

Burns, A. G., Killeen, T. L., Deng, W., Carignan, G. R., & Roble, R. G. (1995). Geomagnetic storm effects in the low-to middle-latitude upper thermosphere. *Journal of Geophysical Research*, *100*(A8), 14673–14691. https://doi.org/10.1029/94ja03232

Burns, A. G., Solomon, S. C., Wang, W., Qian, L., Zhang, Y., Paxton, L. J., et al. (2015). Explaining solar cycle effects on composition as it relates to the winter anomaly. *Journal of Geophysical Research: Space Physics*, *120*(7), 5890–5898. https://doi.org/10.1002/2015JA021220

Cai, X., Qian, L., Wang, W., McInerney, J. M., Liu, H.-L., & Eastes, R. W. (2022a). Investigation of the post-sunset extra electron density peak poleward of the equatorial ionization anomaly southern crest. *Journal of Geophysical Research: Space Physics*, *127*(10), e2022JA030755. https://doi.org/10.1029/2022JA030755

Cai, X., Qian, L., Wang, W., McInerney, J. M., Liu, H.-L., & Eastes, R. W. (2022b). Hemispherically asymmetric evolution of nighttime ionospheric equatorial ionization anomaly in the American longitude sector. *Journal of Geophysical Research: Space Physics*, *127*(11), e2022JA030706. https://doi.org/10.1029/2022JA030706

Chen, J., Zhong, J., Cai, X., Hao, Y., Cai, L., Wan, X., et al. (2024). Characteristics of longitudinal discontinuity over nighttime equatorial ionization anomaly crests with multiple observations. *Journal of Geophysical Research: Space Physics*, *129*(11), e2024JA033133. https://doi.org/10.1029/2024JA033133

Crowley, G., Emery, B. A., Roble, R. G., Carlson, H. C., & Knipp, D. J. (1989). Thermospheric dynamics during September 18–19, 1984: 1. Model simulations. *Journal of Geophysical Research*, *94*(A12), 16925. https://doi.org/10.1029/JA094iA12p16925

Drob, D. P., Emmert, J. T., Meriwether, J. W., Makela, J. J., Doornbos, E., Conde, M., et al. (2015). An update to the Horizontal Wind Model (HWM): The quiet time thermosphere. *Earth and Space Science*, *2*(7), 301–319. https://doi.org/10.1002/2014EA000089

Emmert, J. T., Drob, D. P., Shepherd, G. G., Hernandez, G., Jarvis, M. J., Meriwether, J. W., et al. (2008). DWM07 global empirical model of upper thermospheric storm-induced disturbance winds. *Journal of Geophysical Research*, *113*(A11), A11319. https://doi.org/10.1029/2008JA013541

Emmert, J. T., Fejer, B. G., Fesen, C. G., Shepherd, G. G., & Solheim, B. H. (2001). Climatology of middle- and low latitude F region disturbance neutral winds measured by Wind Imaging Interferometer (WINDII). *Journal of Geophysical Research*, *106*(A11), 24701–24712. https://doi.org/10.1029/2000JA000372

Emmert, J. T., Fejer, B. G., Shepherd, G. G., & Solheim, B. H. (2004). Average nighttime F region disturbance neutral winds measured by UARS WINDII: Initial results. *Geophysical Research Letters*, *31*(22), L22807. https://doi.org/10.1029/2004GL021611

Emmert, J. T., Fejer, B. G., & Sipler, D. P. (2003). Climatology and latitudinal gradients of quiet time thermospheric neutral winds over Millstone Hill from Fabry-Perot interferometer measurements. *Journal of Geophysical Research*, *108*(A5), 1196. https://doi.org/10.1029/2002JA009765

Englert, C. R., Babcock, D. D., & Harlander, J. M. (2007). Doppler asymmetric spatial heterodyne spectroscopy (DASH): Concept and experimental demonstration. *Applied Optics*, *46*(29), 7297–7307. https://doi.org/10.1364/ao.46.007297

Englert, C. R., Harlander, J. M., Brown, C. M., Marr, K. D., Miller, I. J., Stump, J. E., et al. (2017). Michelson Interferometer for Global High-resolution Thermospheric Imaging (MIGHTI): Instrument design and calibration. *Space Science Reviews*, *212*(1), 553–584. https://doi.org/10.1007/s11214-017-0358-4

Englert, C. R., Harlander, J. M., Marr, K. D., Harding, B. J., Makela, J. J., Fae, T., et al. (2023). Michelson interferometer for global high-resolution thermospheric imaging (MIGHTI) on-orbit wind observations: Data analysis and instrument performance. *Space Science Reviews*, *219*(3), 27. https://doi.org/10.1007/s11214-023-00971-1

Fejer, B. G., Emmert, J. T., Shepherd, G. G., & Solheim, B. H. (2000). Average daytime f region disturbance neutral winds measured by uars: Initial results. *Geophysical Research Letters*, *27*(13), 1859–1862. https://doi.org/10.1029/2000gl003787

Fejer, B. G., Emmert, J. T., & Sipler, D. P. (2002). Climatology and storm time dependence of nighttime thermospheric neutral winds over Millstone Hill. *Journal of Geophysical Research*, *107*(A5), 1052. https://doi.org/10.1029/2001JA000300

Fuller-Rowell, T. J. (1998). The 'thermospheric spoon': A mechanism for the semiannual density variation. *Journal of Geophysical Research*, *103*(A3), 3951–3956. https://doi.org/10.1029/97ja03335

Gasperini, F., Forbes, J., Doornbos, E., & Bruinsma, S. L. (2016). Synthetic thermosphere winds based on CHAMP neutral and plasma density measurements. *Journal of Geophysical Research: Space Physics*, *121*(4), 3699–3721. https://doi.org/10.1002/2016JA022392

Gasque, L. C., Harding, B. J., Immel, T. J., Wu, Y.-J., Triplett, C. C., Vadas, S. L., et al. (2024). Evening solar terminator waves in Earth's thermosphere: Neutral wind signatures observed by ICON-MIGHTI. *Journal of Geophysical Research: Space Physics*, *129*(2), e2023JA032274. https://doi.org/10.1029/2023JA032274

Hagan, M., & Forbes, J. (2003). Migrating and nonmigrating semidiurnal tides in the upper atmosphere excited by tropospheric latent heat release. *Journal of Geophysical Research*, *108*(1062), 10.

Hagan, M. E., & Forbes, J. M. (2002). Migrating and nonmigrating diurnal tides in the middle and upper atmosphere excited by tropospheric latent heat release. *Journal of Geophysical Research*, *107*(D24), 4754. https://doi.org/10.1029/2001JD001236

Hays, P., Killeen, T., & Kennedy, B. (1981). The Fabry-Perot interferometer on dynamics explorer. *Space Science Instrumentation*, *5*, 395–416.

Hedin, A. E., Biondi, M. A., Burnside, R. G., Hernandez, G., Johnson, R. M., Killeen, T., et al. (1991). Revised global model of upper thermosphere winds using satellite and ground-based observations. *Journal of Geophysical Research*, *96*(A5), 7657–7688. https://doi.org/10.1029/91JA00251

Hedin, A. E., Spencer, N. W., & Killeen, T. L. (1988). Empirical global model of upper thermosphere winds based on atmosphere and dynamics explorer satellite data. *Journal of Geophysical Research*, *93*(A9), 9959–9978. https://doi.org/10.1029/JA093iA09p09959

Hsu, V. W., Thayer, J. P., Wang, W., & Burns, A. (2016). New insights into the complex interplay between drag forces and its thermospheric consequences. *Journal of Geophysical Research: Space Physics*, *121*(10), 10417–10430. https://doi.org/10.1002/2016JA023058

Immel, T. J., England, S. L., Mende, S. B., Heelis, R. A., Englert, C. R., Edelstein, J., et al. (2017). The ionospheric connection ex-plorer mission: Mission goals and design. *Space Science Reviews*, *214*(1), 13. https://doi.org/10.1007/s11214-017-0449-2

Jiang, G., Xiong, C., Stolle, C., Xu, J., Yuan, W., Makela, J. J., et al. (2021). Comparison of thermospheric winds measured by GOCE and ground-based FPIs at low and middle latitudes. *Journal of Geophysical Research: Space Physics*, *126*(2), e2020JA028182. https://doi.org/10.1029/2020JA028182

Jiang, G., Xu, J., Wang, W., Yuan, W., Zhang, S., Yu, T., et al. (2018). A comparison of quiet time thermospheric winds between FPI observations and model calculations. *Journal of Geophysical Research*, *123*(9), 7789–7805. https://doi.org/10.1029/2018JA025424

Jones, M., Jr., Forbes, J. M., & Hagan, M. E. (2016). Solar cyclevariability in mean thermospheric composition and temperature induced by atmospheric tides. *Journal of Geophysical Research: Space Physics*, *121*(6), 5837–5855. https://doi.org/10.1002/2016JA022701

Kelley, M. C. (2009). *The Earth's ionosphere: Plasma physics & electrodynamics* (2nd ed., Vol. 96). Academic Press.

Killeen, T. L., & Roble, R. G. (1984). An analysis of the high-latitude thermospheric wind pattern calculated by a thermospheric general circulation model: 1. Momentum forcing. *Journal of Geophysical Research*, *89*(A9), 7509–7522. https://doi.org/10.1029/JA089iA09p07509

Killeen, T. L., & Roble, R. G. (1986). An analysis of the high-latitude thermospheric wind pattern calculated by a thermospheric general circulation model: 2. Neutral parcel transport. *Journal of Geophysical Research*, *91*(A10), 11291–11307. https://doi.org/10.1029/JA091IA10P11291

Kuai, J., Ma, Q., Yu, T., Wu, K., Sun, H., & Zhang, Y. (2025). Significant east-west electron density differences occurring in less than 30° longitude over the ocean during the recovery phase of a strong geomagnetic storm in solar minimum. *Journal of Geophysical Research: Space Physics*, *130*, e2024JA033549. https://doi.org/10.1029/2024JA033549

Kwak, Y.-S., & Richmond, A. D. (2007). An analysis of the momentum forcing in the high-latitude lower thermosphere. *Journal of Geophysical Research*, *112*(A1), A01306. https://doi.org/10.1029/2006JA011910

Larsen, M. F., & Mikkelsen, I. S. (1983). The dynamic response of the high-latitude thermosphere and geostrophic adjustment. *Journal of Geophysical Research*, *88*(A4), 3158–3168. https://doi.org/10.1029/ja088ia04p03158

Lei, J., Roble, R. G., Kawamura, S., & Fukao, S. (2007). A simulation study of thermospheric neutral winds over the MU radar. *Journal of Geophysical Research*, *112*(A4), A04303. https://doi.org/10.1029/2006JA012038

Liu, H., Lu¨hr, H., Watanabe, S., Kohler, W., Henize, V., & Visser, P. (2006). Zonal winds in the equatorial upper thermosphere: Decomposing the solar flux, geomagnetic activity, and seasonal dependencies. *Journal of Geophysical Research*, *111*(A7), A07307. https://doi.org/10.1029/2005JA011415

Liu, L., Luan, X., Wan, W., Lei, J., & Ning, B. (2003). Seasonal behavior of equivalent winds over Wuhan derived from ionospheric data in 2000 - 2001. *Advances in Space Research*, *32*(9), 1765–1770. https://doi.org/10.1016/s0273-1177(03)90474-1

Liu, L., Luan, X., Wan, W., Lei, J., & Ning, B. (2004). Solar activity variations of equivalent winds derived from global ionosonde data. *Journal of Geophysical Research*, *109*(A12), A12305. https://doi.org/10.1029/2004JA010574

Luan, X., Liu, L., Wan, W., Lei, J., & Yu, T. (2004). Climatology of the F-layer equivalent winds derived from ionosonde measurements over two decades along the 120°–150°E sector. *Annals of Geophysics*, *22*(8), 2785–2796. https://doi.org/10.5194/angeo-22-2785-2004

Luan, X., & Solomon, S. C. (2008). Meridional winds derived from COSMIC radio occultation measurements. *Journal of Geophysical Research*, *113*(A8), A08302. https://doi.org/10.1029/2008JA013089

Makela, J. J., Baughman, M., Navarro, L. A., Harding, B. J., Englert, C. R., Harlander, J. M., et al. (2021). Validation of ICON-MIGHTI thermospheric wind observations: 1. Nighttime Red-line Ground-Based Fabry-Perot Interferometers. *Journal of Geophysical Research: Space Physics*, *126*(2). https://doi.org/10.1029/2020JA028726

Mikkelsen, I. S., & Larsen, M. F. (1983). An analytic solution for the response of the neutral atmosphere to the high-latitude convection pattern. *Journal of Geophysical Research*, *88*(A10), 8073–8080. https://doi.org/10.1029/ja088ia10p08073

Oberheide, J., Forbes, J. M., Zhang, X., & Bruinsma, S. L. (2011). Climatology of upward propagating diurnal and sem-diurnal tides in the thermosphere. *Journal of Geophysical Research*, *116*(A11), A11306. https://doi.org/10.1029/2011JA016784

Qian, L., Burns, A. G., Emery, B. A., Foster, B., Lu, G., Maute, A., et al. (2014). The NCAR TIE-GCM. In *Modeling the ionosphere- thermosphere system* (pp. 73–83). American Geophysical Union. https://doi.org/10.1002/9781118704417.ch7

Qian, L., Burns, A. G., Wang, W., Solomon, S. C., Zhang, Y., & Hsu, V. (2016). Effects of the equatorial ionosphere anomaly on the interhemispheric circulation in the thermosphere. *Journal of Geophysical Research: Space Physics*, *121*(3), 2522–2530. https://doi.org/10.1002/2015JA022169

Richmond, A. D. (1989). Modeling the ionosphere wind dynamo: A review. *PAGEOPH*, *131*(3), 413–435. https://doi.org/10.1007/BF00876837

Richmond, A. D., Ridley, E. C., & Roble, R. G. (1992). A thermosphere/ionosphere general circulation model with coupled electrodynamics. *Geophysical Research Letters*, *19*(6), 369–604. https://doi.org/10.1029/92gl00401

Richmond, A. D., & Roble, R. G. (1987). Electrodynamic effects of thermospheric winds from the NCAR thermospheric general circulation model. *Journal of Geophysical Research*, *92*(A11), 12365–12376. https://doi.org/10.1029/ja092ia11p12365

Rishbeth, H. (1998). How the thermospheric circulation affects the ionospheric F2-layer. *Journal of Atmospheric and Solar-Terrestrial Physics*, *60*(14), 1385–1402. https://doi.org/10.1016/s1364-6826(98)00062-5

Rishbeth, H., & Müller-Wodarg, I. C. F. (1999). Vertical circulation and thermospheric composition: A modelling study. *Annals of Geophysics*, *17*(6), 794–805. https://doi.org/10.1007/s005850050808

Roble, R. G., Ridley, E. C., Richmond, A. D., & Dickinson, R. E. (1988). A coupled thermosphere/ionosphere general circulation model. *Geophysical Research Letters*, *15*(12), 1325–1328. https://doi.org/10.1029/GL015i012p01325

Shepherd, G. G., Thuillier, G., Gault, W. A., Solheim, B. H., Hersom, C., Alunni, J. M., et al. (1993). WINDII, the wind imag-ing interferometer on the Upper Atmosphere Research Satellite. *Journal of Geophysical Research*, *98*(D6), 10725–10750. https://doi.org/10.1029/93JD00227

Spencer, N., Wharton, L., Carignan, G., & Maurer, J. (1982). Thermosphere zonal winds, vertical motions and temperature as measured from-Dynamics Explorer. *Geophysical Research Letters*, *9*(9), 953–956. https://doi.org/10.1029/gl009i009p00953

Wang, W., Burns, A. G., Wiltberger, M., Solomon, S. C., & Killeen, T. L. (2008). Altitude variations of the horizontal thermospheric winds during geomagnetic storms. *Journal of Geophysical Research*, *113*(A2), A02301. https://doi.org/10.1029/2007JA012374

Weimer, D. R. (2005). Improved ionospheric electrodynamic models and application to calculating Joule heating rates. *Journal of Geophysical Research*, *110*(A5), A05306. https://doi.org/10.1029/2004JA010884

Wu, K., Qian, L., Wang, W., Cai, X., & Mclnerney, J. M. (2023). Investigation of the GOLD observed merged nighttime EIA with WACCM-X simulations during the storm of 3 and 4 November 2021. *Geophysical Research Letters*, *50*(13), e2023GL103603. https://doi.org/10.1029/2023GL103603

Wu, K., Qian, L., Wang, W., Cai, X., & Mclnerney, J. M. (2025). The formation mechanism of merged EIA during a storm on 4 November 2021. *Journal of Geophysical Research: Space Physics*, *130*, e2024JA032896. https://doi.org/10.1029/2024JA032896

Xiong, C., Lühr, H., & Fejer, B. G. (2016). The response of equatorial electrojet, vertical plasma drift, and thermospheric zonal wind to enhanced solar wind input. *Journal of Geophysical Research: Space Physics*, *121*(6), 5653–5663. https://doi.org/10.1002/2015JA022133

Yamazaki, Y., Harding, B. J., Qiu, L., Stolle, C., Siddiqui, T. A., Miyoshi, Y., et al. (2023). Monthly climatologies of zonal-mean and tidal winds in the thermosphere as observed by ICON/MIGHTI during April 2020–March 2022. *Earth and Space Science*, *10*(6), e2023EA002962. https://doi.org/10.1029/2023EA002962

Yamazaki, Y., & Richmond, A. D. (2013). A theory of ionospheric response to upward-propagating tides: Electrodynamic effects and tidal mixing effects. *Journal of Geophysical Research: Space Physics*, *118*(9), 5891–5905. https://doi.org/10.1002/jgra.50487

Yiğit, E., Dhadly, M., Medvedev, A. S., Harding, B. J., Englert, C. R., Wu, Q., & Immel, T. J. (2022). Characterization of the thermospheric mean winds and circulation during solstice using ICON/MIGHTI observations. *Journal of Geophysical Research: Space Physics*, *127*(11), e2022JA030851. https://doi.org/10.1029/2022JA030851

Yu, T. (2024). Local time variations of quiet time meridional winds during solar minimum solstices based on ICON observations and numerical simulations [Dataset]. *Zenodo*. https://doi.org/10.5281/zenodo.13932409

Yu, T., Cai, X., Ren, Z., Li, S., Pedatella, N., & He, M. (2022). Investigation of the ΣO/N2 depletion with latitudinally tilted equatorward boundary observed by GOLD during the geomagnetic storm on April 20, 2020. *Journal of Geophysical Research: Space Physics*, *127*(12), e2022JA030889. https://doi.org/10.1029/2022JA030889

Yu, T., Cai, X., Ren, Z., Wang, Z., Pedatella, N. M., & Jin, Y. (2023). Investigation of interhemispheric asymmetry of the thermospheric composition observed by GOLD during the first strong geomagnetic storm in solar-cycle 25, 1: IMF B_y effects. *Journal of Geophysical Research: Space Physics*, *128*(10), e2023JA031429. https://doi.org/10.1029/2023JA031429

Yu, T., Ren, Z., Le, H., Wan, W., Wang, W., Cai, X., & Li, X. (2020). Seasonal variation of O/N2 on different pressure levels from GUVI limb measurements. *Journal of Geophysical Research: Space Physics*, *125*(8), e2020JA027844. https://doi.org/10.1029/2020JA02784

Yu, T., Wan, W., Liu, L., & Zhao, B. (2004). Global scale annual and semi-annual variations of daytime NmF2 in the high solar activity years. *Journal of Atmospheric and Solar-Terrestrial Physics*, *66*(18), 1691–1701. https://doi.org/10.1016/j.jastp.2003.09.018

Yu, T., Wang, W., Ren, Z., Cai, X., Yue, X., & He, M. (2021). The response of middle thermosphere (∼160 km) composition to the 20-21 November 2003 superstorm. *Journal of Geophysical Research: Space Physics*, *126*(10). https://doi.org/10.1029/2021ja029449

Yu, T., Wang, W., Ren, Z., Yue, J., Yue, X., & He, M. (2021). Middle-low latitude neutral composition and temperature responses to the 20 and 21 November 2003 superstorm from GUVI dayside limb measurements. *Journal of Geophysical Research: Space Physics*, *126*(8), 1–13. https://doi.org/10.1029/2020ja028427

Zhai, C., Cai, X., Yu, T., Peng, W., Cheng, X., Yue, D., & Cai, L. (2024). A complete chain of the generating processes of ionospheric negative storm over the North America. *Journal of Geophysical Research: Space Physics*, *129*(9), e2024JA033091. https://doi.org/10.1029/2024JA033091

Zhang, K., Wang, W., Wang, H., Dang, T., Liu, J., & Wu, Q. (2018). The longitudinal variations of upper thermospheric zonal winds observed by the CHAMP satellite at low and midlatitudes. *Journal of Geophysical Research: Space Physics*, *123*(11), 9652–9668. https://doi.org/10.1029/2018JA025463